Monthly Notices
of the
ROYAL ASTRONOMICAL SOCIETY
MNRAS **445,** 1403–1411 (2014) doi:10.1093/mnras/stu1819

Swift J2218.4+1925: a new hard-X-ray-selected polar observed with *XMM–Newton*

F. Bernardini,[1,2]★ D. de Martino,[2] K. Mukai[3,4] and M. Falanga[5,6]

[1] *Wayne State University, 666 W. Hancock Street, Detroit, MI 48201, USA*
[2] *INAF – Osservatorio Astronomico di Capodimonte, Salita Moiariello 16, I-80131 Napoli, Italy*
[3] *CRESST and X-Ray Astrophysics Laboratory, NASA Goddard Space Flight Center, Greenbelt, MD 20771, USA*
[4] *Department of Physics, University of Maryland, Baltimore County, 1000 Hilltop Circle, Baltimore, MD 21250, USA*
[5] *International Space Science Institute (ISSI), Hallerstrasse 6, CH-3012 Bern, Switzerland*
[6] *International Space Science Institute Beijing, No. 1 Nan Er Tiao, Zhong Guan Cun, Beijing 100190, China*

Accepted 2014 September 2. Received 2014 September 1; in original form 2014 June 9

ABSTRACT

Swift J2218.4+1925, a hard-X-ray source detected by *Swift* Burst Alert Telescope (BAT), has been proposed as a candidate magnetic cataclysmic variable of the polar type from optical spectroscopy. Using *XMM–Newton* we perform detailed timing and spectral analysis with simultaneous X-ray (0.3–10 keV) and optical *B*-band data. We complement the spectral study with archival hard-X-ray (14–70 keV) spectra collected by *Swift* BAT as well as with optical, near and mid-infrared photometry from Sloan Digital Sky Survey, Two-Micron All Sky Survey and *Wide-field Infrared Survey Explorer* archive, respectively. A strong periodic X-ray signal at 2.16 h, fully consistent with the recently determined spectroscopic orbital period, adds Swift J2218.4+1925 to the small group of hard-X-ray polars and locates it at the low edge of the orbital period gap. The X-ray pulse profile shows the typical bright and faint phases seen in polars, that last ∼70 and ∼30 per cent of the orbit, respectively. A pronounced dip centred on the bright phase is also detected. It is stronger at lower energies and is mainly produced by photoelectric absorption. A binary inclination $i \sim 40^\circ$–50° and a magnetic colatitude $\beta \sim 55^\circ$–64° are estimated. The source appears to accrete over a large area ∼24° wide. A multitemperature optically thin emission with complex absorption well describes the broad-band (0.3–70 keV) spectrum, with no signs of a soft X-ray blackbody component. The spectral shape strongly varies with the source rotation reaching plasma temperatures up to 55 keV, hardening at the dip and being softer during the faint phase (∼7 keV). We also find the first indication of an absorption edge due to a warm absorber in a polar. Indication of overabundance of neon is found in the Reflection Grating Spectrometer (RGS) spectra. The UV to mid-IR spectral energy distribution reveals an excess in the near and mid-IR, likely due to low cyclotron harmonics. We further estimate a white dwarf mass of 0.97 $M_\odot$ and a distance of 230–250 pc.

Key words: novae, cataclysmic variables – white dwarfs – X-rays: individual: Swift J2218.4+1925.

1 INTRODUCTION

Cataclysmic Variable stars (CVs) are X-ray binaries hosting a white dwarf (WD) that is accreting matter from a companion star (a late-type main-sequence or a sub-giant) with mass smaller than that of the Sun. The *Swift* Burst Alert Telescope (BAT; Barthelmy 2000) and *INTEGRAL* IBIS (Ubertini et al. 2003) surveys detected a non-negligible number of new CVs (Bird et al. 2010; Cusumano et al. 2010; Baumgartner et al. 2013). Most of the known hard-X-ray-detected CVs are magnetic CVs of the intermediate polar type (Barlow et al. 2006), a few are instead polars. The first host asynchronously ($P_{\rm rot} < P_{\rm orb}$) rotating WDs with possibly weaker magnetic fields ($B \leq 10^6$ G), while the latter contain synchronously ($P_{\rm rot} = P_{\rm orb}$) rotating WDs with stronger magnetic fields, $B \sim 10$–230×10^6 G (see also Warner 1995, for a review). The incidence of magnetism in the hard-X-ray-selected samples is very high, up to ∼90 per cent. Magnetic CVs, especially the intermediate polars, are debated to represent the main constituent of the Galactic population of X-ray sources at low luminosities (Muno et al. 2004; Sazonov et al. 2006; Revnivtsev et al. 2009, 2011). Newly dis-

★ E-mail: bernardini@wayne.edu

covered sources identified through optical photometry (e.g. Masetti et al. 2008, 2010, 2012a; Masetti, Nucita & Parisi 2012b) have added as candidates to the group of magnetic CVs. However, the proper identification and classification of new sources relies on X-rays, as successfully demonstrated in the recent years (e.g. Anzolin et al. 2008, 2009; de Martino et al. 2008; Bernardini et al. 2012, 2013), that indeed reveal that most of the hard-X-ray CV candidates are of the magnetic type. We here present the results of a dedicated *XMM–Newton* pointing to assess the true nature of the new hard-X-ray-selected source, Swift J2218.4+1925.

Swift J2218.4+1925 was detected by the BAT instrument on board *Swift* and is coincident with 1RXS J221832.8+192527. Using optical time-resolved spectroscopy, Thorstensen & Halpern (2013) derived an orbital period of 7773 ± 7 s. The broad wings and the large amplitude of radial velocities of the Hα emission line also suggested a magnetic nature for this CV. The additional presence of a narrow component in the emission line profiles, antiphased with respect to the broad component, and ascribed to the irradiated face of the secondary star, further suggested a polar-type magnetic CV. However, the detection of X-ray pulsations at a period consistent with that of orbital spectroscopy, as well as optical polarimetry are mandatory to confirm the classification. Up to now Swift J2218.4+1925 was observed in the soft-X-ray range (<10 keV) only sporadically with the X-ray Telescope instrument on board *Swift* and no X-ray periodicity was found (Thorstensen & Halpern 2013). *XMM–Newton* has proven to be the best observatory, currently operating, to identify periodic signals on the time-scales exhibited by CVs (minutes–hours) and to characterize their spectral properties (see e.g. Bernardini et al. 2012, 2013). In Section 2, we present the *XMM–Newton* data complemented with the *Swift* BAT data. In Section 3, we present the X-ray results together with optical, near and mid-infrared photometry from the Sloan Digital Sky Survey (SDSS), the Two-Micron All Sky Survey (2MASS) and the *Wide-field Infrared Survey Explorer* (*WISE*; Wright et al. 2010). The results are discussed in Section 4, in terms of emission components.

2 OBSERVATIONS AND DATA ANALYSIS

2.1 *XMM–Newton* observations

Swift J2218.4+1925 was observed in 2013 November by *XMM–Newton* observatory (den Herder et al. 2001; Mason et al. 2001; Turner et al. 2001) with the European Photon Imaging Camera (EPIC) (PN, MOS1 and MOS2) as main instruments. The details of the observation, together with that of *Swift* are reported in Table 1. The *XMM–Newton* data were processed using the SAS version 13.0.0 and the latest calibration files (CCF) available in 2013 October.

2.1.1 *The EPIC and RGS data*

The three EPIC cameras were all set in Prime Full Window imaging mode with the thin filter applied. Standard data screening criteria were applied for all instruments. For the EPIC data, we extracted the source photons from a circular region of radius 37.5 arcsec centred at the source position. Background photons were taken from a nearby region of the sky of radius 70 arcsec, clear from source contamination, in the same CCD where the source lies. For the spectral analysis, in order to avoid background solar flare contamination, we generated the source and the background spectra removing high background epochs in all three instruments. For the timing analysis, instead, we used the whole data set. We also produced background-subtracted light curves in the ranges 0.3–12 keV (with a bin time of 15 s), 0.3–1 keV, 1–3 keV, 3–5 keV and 5–12 keV (with a bin time of 75 s). The event arrival times were corrected to Solar system barycentre by using the task BARYCEN. The average (whole observation) EPIC spectra were rebinned before fitting in order to have a minimum of 25 counts each bin. Spectra were also extracted as a function of the source rotational phase (pulse–phase spectroscopy analysis). We report the spectral results of the simultaneous analysis of the three cameras in order to increase the signal to noise (S/N). The spectral fit were made with XSPEC version 12.7.1.

The two Reflection Grating Spectrometer (RGS) instruments were operated in Spectroscopy mode. The source is quite faint, with the net count rates reported in Table 1 corresponding to 56 and 67 per cent of the total (source plus background) count rates for RGS1 and RGS2, respectively.

2.1.2 *The optical monitor photometry*

The Optical Monitor (OM) instrument, operated in fast window mode, observed Swift J2218.4+1925 with the *B* filter, centred at 4500 Å, simultaneously to the EPIC cameras. A total of 10 series of ∼2800 s were obtained (see Table 1). Swift J2218.4+1925 is found at an average magnitude $B = 17.8 \pm 0.05$ corresponding to a flux $4.80 \pm 0.06 \times 10^{-16}$ erg cm^{-2} s^{-1} Å^{-1}. It is at similar flux level as when detected in the SDSS, $g' = 17.64 \pm 0.01$ and when observed by Thorstensen & Halpern (2013), both in 2009. The OM light curves as obtained from the standard processing pipeline were also corrected to the Solar system barycentre.

2.2 The *Swift* observations

BAT is sensitive in the 14–195 keV energy range and has built up an all-sky map of the hard X-ray sky thanks to its wide field of view. We downloaded the eight-channel spectra

Table 1. Summary of main observations parameters for all instruments. Uncertainties are at 1σ confidence level.

Telescope	OBSID	Instrument	Date yy-mm-dd	UT_{start} hh:mm	T^a_{expo} (ks)	Net source count rate (c s^{-1})
XMM–Newton	0721790101	EPIC-pn	2013-11-25	19:47	31.5	1.263 ± 0.007
		EPIC-MOS1	2013-11-25	19:24	33.1	0.359 ± 0.03
		EPIC-MOS2	2013-11-25	19:24	33.1	0.361 ± 0.03
		RGS1	2013-11-25	19:23	33.4	0.0184 ± 0.0012^b
		RGS2	2013-11-25	19:23	33.4	0.0257 ± 0.0012^b
		OM-B	2013-11-25	19:30	28.0	3.85 ± 0.02
Swift	[c]	BAT			1×10^7	$1.6 \pm 0.3 \times 10^{-5}$

Note: [a]Net exposure times. [b]We report the net count rate in the 0.4–2.0 keV band, excluding dead channels. [c]All available pointings collected during 2004 December to 2010 September are summed together.

from the first 70 month of monitoring directly available at http://swift.gsfc.nasa.gov/results/bs70mon/.

3 RESULTS

3.1 The X-ray timing analysis

The 0.3–12 keV background-subtracted PN light curve is shown in Fig. 1. A periodic modulation is evident (the observation covers four cycles), showing a bright double-humped pulse. The power spectrum in the 0.3–12 keV range reveals a strong peak at $\sim 1.3 \times 10^{-4}$ Hz together with harmonics up to the fourth. A period $P = 7770 \pm 10$ was determined by fitting the PN 0.3–12 keV light curve with a composite sinusoidal function with the fundamental frequency plus its first four harmonics. This is consistent within 1σ with the period derived from optical spectroscopy (7773 ± 7 s Thorstensen & Halpern 2013). All uncertainties are hereafter at 1σ confidence level if not otherwise specified.

We folded the background-subtracted light curves at $P = 7770$ s. They show a relatively long (70 per cent) bright phase and a faint phase ($\sim$30 per cent), where the count rate goes close to zero only for $E > 3$ keV. The bright phase is characterized by a double-humped maximum with a slightly stronger first peak and a prominent dip between the two (see Fig. 2). The pulse profile structure slightly evolves with energy, and the dip is clearly more pronounced at lower energies. To measure the fractional intensity of the dip (ΔI) we fit the pulse bright phase in the range 0.4–0.9 with a linear function, accounting for the overall decay in the count rate in this range, plus a Gaussian accounting for the dip. We left the intensity of the Gaussian (I), the semihalf-width at half-intensity (σ) and the phase centre ($\phi_{\rm cent}$) free to vary. We then define the fractional intensity of the dip: $\Delta I = I/I_{\rm cent}$, where $I_{\rm cent}$ is the interpolated continuum count rate evaluated at the dip centre. We find: ΔI is 85 ± 8 per cent (0.3–1 keV), 76 ± 6 per cent (1–3 keV), 38 ± 5 per cent (3–5 keV) and 12 ± 4 per cent (5–12 keV).

We also inspected the times of dip occurrence during the four cycles covered by the *XMM–Newton* observation (see Fig. 1). The first and third dip occur at similar phase while the second is leading by 30 ± 15 s and the fourth is delayed by 110 ± 15 s. This is not evidence of period change, but rather a signature of changes or oscillation in the accretion flow rate. This behaviour is not uncommon in polars (Harrop-Allin et al. 1999; Schwope et al. 2001).

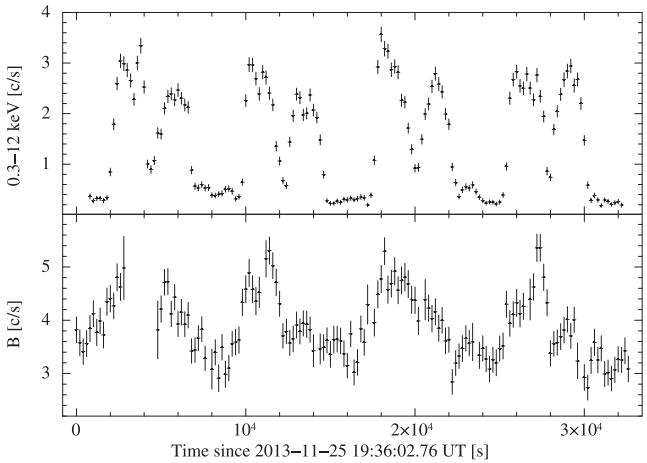

Figure 1. Upper panel: 0.3–12 keV background-subtracted PN light curve. Lower panel: optical B-band light curve. The binning time is 200 s.

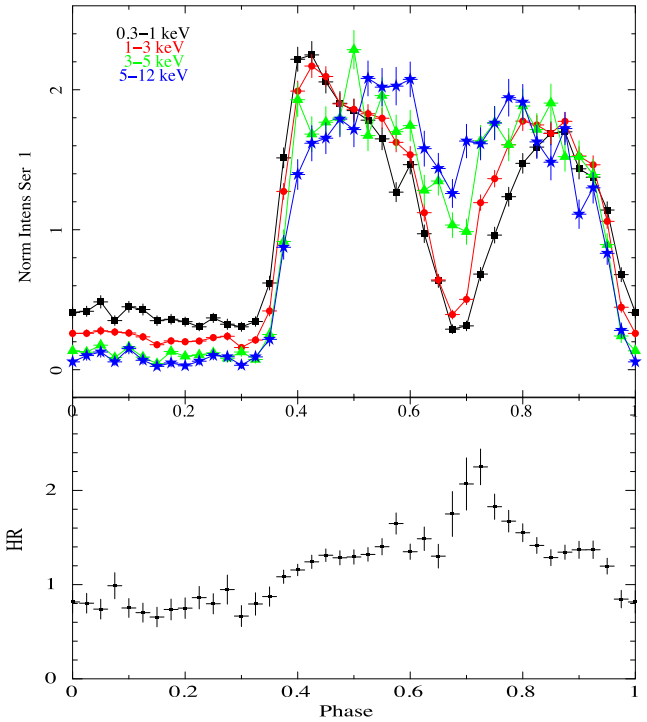

Figure 2. Upper panel: PN background-subtracted light curves, folded at $P = 7770$ s, in four energy intervals: 0.3–1 (black squares), 1–3 (red circles), 3–5 (green triangles), 5–12 (blue stars) keV. Lower panel: hardness ratio, 1–3 keV versus0.3–1 keV.

We also calculated the pulsed fraction (PF) of the fundamental harmonic here defined as $\mathrm{PF} = (A_{\rm max} - A_{\rm min})/(A_{\rm max} + A_{\rm min})$. $A_{\rm max}$ and $A_{\rm min}$ are the maximum and minimum value of the sinusoid used to fit the fundamental harmonic. The PF increases with the energy interval being $\mathrm{PF}_{0.3-1\,\rm keV} = 49 \pm 1$ per cent, $\mathrm{PF}_{1-3\,\rm keV} = 68.9 \pm 0.8$ per cent, $\mathrm{PF}_{3-5\,\rm keV} = 95 \pm 1$ per cent, $\mathrm{PF}_{5-12\,\rm keV} = 102 \pm 1$ per cent. We also inspected the spectral behaviour versus phase measuring the hardness ratio (HR) defined as $\mathrm{HR} = n^{\phi}_{\rm keV^a}/n^{\phi}_{\rm keV^b}$, where $n^{\phi}_{\rm keV}$ is the number of photons in the inspected energy range (called a and b), and ϕ is the phase interval. We found a strong hardening at the phase corresponding to the dip ($\phi \sim 0.7$) for both $\mathrm{HR} = n^{\phi}_{1-3}/n^{\phi}_{0.3-1}$ and $\mathrm{HR} = n^{\phi}_{3-5}/n^{\phi}_{1-3}$ (see Fig. 2).

3.2 The optical timing analysis

A fit made with a single sinusoid to the B-band light curve gives a period of 7834 ± 44 s, consistent within 1.5σ with that found from X-rays. The shape of the pulse profile is similar to that in the X-rays, but with a slower rise to the maximum and a much weaker secondary maximum. The intensity of the pulsation, $\mathrm{PF_B} = 16.8 \pm 0.7$ per cent, is much lower than in the 0.3–12 keV band, $\mathrm{PF}_{0.3-12\,\rm keV} = 79.2 \pm 0.5$ per cent (see Fig. 3). A cross-correlation between X-ray (0.3–12 keV) and B-band light curves gives the optical leading the X-ray light by $\sim$700 s. This is mainly dictated by the early rise to the maximum with respect to the X-rays.

The B-band pulse also reveals an optical counterpart of the X-ray dip that is also occurring at $\phi \sim 0.7$, but with a slower decay. We found $\Delta I_B = 18 \pm 3$ per cent, which is similar to that of the 5–12 keV range ($\Delta I = 12 \pm 4$ per cent), but much lower than that in the 0.3–1 keV range ($\Delta I = 85 \pm 8$ per cent). The dip has a width of about 0.1 in phase, both in the X-ray and in the B band.

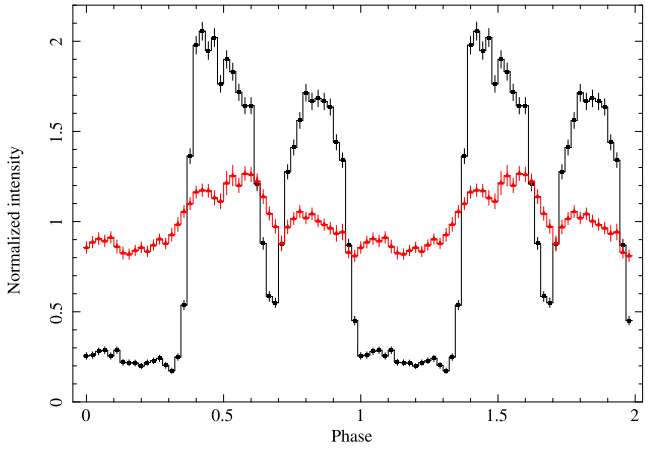

Figure 3. X-ray (0.3–12 keV, black circles) versus optical (B, red triangles) folded light curves. The folding period is 7770 s. The two folded light curves are over-plotted to allow direct comparison. Two cycles are shown for plotting purposes.

3.3 X-ray spectral analysis

We simultaneously fitted the average spectrum of the three EPIC cameras together with that of BAT. A single temperature model is inadequate to fit the resulting broad-band (0.3–70 keV) spectrum. The best-fitting model is a combination of a multitemperature-like optically thin plasma (CEMEKL) plus a Gaussian at 6.4 keV (emission line), including a total (PHABS) and a partial covering (PCFABS) absorber. They account for the absorptions from the Galactic interstellar medium and from a local, partial covering, cool material close to the source. We linked all model parameters among different instruments, leaving free to vary only a normalization parameter accounting for a possible difference in the calibration. The CEMEKL model is normally used to account for a gradient of temperature in the post-shock region of CVs. The emission measure follows a power law in temperature $\mathrm{d\,EM} = (T/T_{\rm max})^{a-1}\,\mathrm{d}T/T_{\rm max}$. We obtained $kT_{\rm max} = 37 \pm 7$ keV and $\alpha = 1.1 \pm 0.1$. The total absorber column density, $N_{\rm H_P} = 3.3 \pm 0.3 \times 10^{20}$ cm^{-2}, is lower than the Galactic value in the direction of the source (4.4–4.8 $\times\ 10^{20}$ cm^{-2}) derived from Kalberla et al. (2005) and Dickey & Lockman (1990), implying an origin in the Galactic interstellar medium. On the other hand, the partial covering absorption component has $N_{\rm H_{pc}} = 4.8 \pm 0.5 \times 10^{22}$ cm^{-2} and a covering fraction cvf $= 42 \pm 2$ per cent, implying a localized origin. The fluorescent Fe 6.4 keV emission line has an equivalent width EW $= 0.10 \pm 0.02$ keV. We also noticed in the fit residual the presence of a feature in all three instruments (see Fig. 4 lower panel) and we modelled it with an EDGE. The EDGE parameters were linked between different instruments, but left free to vary to minimize the χ^2. We measure $E_{\rm edge} = 0.69 \pm 0.01$ keV, and $\tau_{\rm edge} = 0.35 \pm 0.06$, where $E_{\rm edge}$ is the threshold energy and $\tau_{\rm edge}$ the absorption depth at the threshold. The fit has $\chi^2 = 1324.63$ for 1299 degrees of freedom (dof), compared to $\chi^2 = 1371.08$ for 1301 dof, for the fit without the EDGE. All spectral parameters are reported in Table 2, and the average spectrum is shown in Fig. 4. We stress that the feature is simultaneously detected in the PN, MOS1 and MOS2 spectra and that $\Delta\chi^2$ is quite high (46.45). This points towards a real detection more than to a feature produced by a random statistical fluctuation.

In order to properly estimate the significance of the absorption feature we run extensive Monte Carlo simulation by producing 10^4 spectra for each instrument (PN, MOS1 and MOS2) using as underling continuum the best-fitting model used for the average spectrum, without the EDGE (see e.g. Bernardini et al. 2009; Lanzuisi et al. 2013, for more details on the technique). The simulated spectra have the same continuum flux, background flux and exposure as observed. We first fitted the simulated spectra with the best-fitting model without the EDGE, and then with the same model including the EDGE. The EDGE energy was left free to vary in the full 0.3–10 keV energy range. Also $\tau_{\rm edge}$ was left free to minimize the χ^2. Then, we counted how many times we obtained a $\Delta\chi^2$ greater than the observed one (46.45), just because of statistical fluctuations. Since we never found a $\Delta\chi^2$ greater than the observed one, this implies that we found 0 spectra over 10^4 set of PN and MOSs spectra

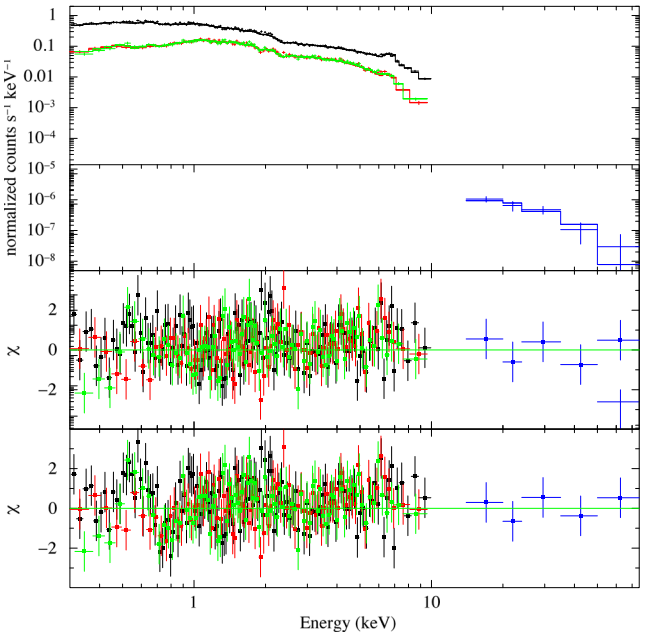

Figure 4. Upper panel: broad-band 0.3–100 keV spectrum of Swift J2218.4+1925. The PN spectrum is shown in black, the MOS1 and MOS2 spectra are in red and green, respectively, while the BAT spectrum is in blue. The continuum lines represent the best-fitting model. Central panel: post-fit residuals with respect to the best-fitting model including the EDGE. Lower panel: post-fit residuals without the inclusion of the EDGE.

Table 2. Spectral parameters for the best-fitting model. We also report the absorbed/(unabsorbed) 0.3–10 keV ($F_{0.3-10}$) flux and the unabsorbed 15–70 (F_{15-70}), and 0.3–100 ($F_{\rm bol}$) keV fluxes. Uncertainties are at the 1σ confidence level.

Average spectrum		
$N_{\rm H_P}$	10^{22} cm^{-2}	0.033 ± 0.003
$N_{\rm H_{pc}}$	10^{22} cm^{-2}	4.8 ± 0.5
cvf	per cent	42 ± 2
$E_{\rm edge}$	keV	0.69 ± 0.01
$\tau_{\rm edge}$		0.35 ± 0.06
$kT_{\rm max}$	keV	37 ± 7
α	1.1 ± 0.1	
norm	10^{-2}	0.9 ± 0.1
A_Z		0.71 ± 0.09
EW^a	keV	0.10 ± 0.02
$F_{0.3-10}$	10^{-12} erg cm^{-2} s^{-1}	6.05 ± 0.05 ($\sim$7.8)
F_{15-70}	10^{-12} erg cm^{-2} s^{-1}	$6.4\pm^{0.8}_{1.3}$
$F_{\rm bol}$	10^{-12} erg cm^{-2} s^{-1}	$\sim$16
χ^2_ν (dof)		1.02 (1299)

Note: [a]Gaussian energy fixed at 6.4 keV.

presenting such intense absorption feature just because of statistical fluctuations. This leads to an estimated significance level greater than 3.9σ for the 0.7 keV edge.

A blackbody component with $kT \sim 20$–60 eV has been one of the defining X-ray spectral characteristics of the polar-type CVs. However, the 3σ upper limit on the unabsorbed 0.3–10 keV flux of this soft blackbody, even in absence of the edge, is only 1×10^{-17} erg cm^{-2} s^{-1}. We conclude that this component is not statistically required in the fit. The reason for the absence of this component is discussed in Section 4.

3.3.1 *Pulse phase spectroscopy*

We also analysed the 0.3–10 keV *XMM–Newton* spectrum as a function of the rotational phase. We selected four phase intervals corresponding to: the minimum ($\phi = 0.00$–0.31), the first maximum ($\phi = 0.39$–0.61), the dip ($\phi = 0.63$–0.70) and the second maximum ($\phi = 0.76$–0.93) of the pulse profile (see Fig. 3). We fitted simultaneously the spectra of the three EPIC cameras using the best-fitting average spectral model by linking all the model components with the exception of the normalization accounting for a possible difference in the calibration. We fixed the interstellar absorption, the abundance and α to their average spectral value. All model parameters are reported in Table 3. We found that the spectral properties significantly change with the phase. The spectrum at phase minimum is characterized by a cooler emitting region (see also Fig. 5). We found $kT_{\rm max} = 6.3 \pm 0.7$, $kT_{\rm max} = 55 \pm 10$, $kT_{\rm max} = 44\pm^{50}_{16}$ and $kT_{\rm max} = 43\pm^{12}_{8}$ keV for the minimum, first maximum, dip and second maximum, respectively. The $N_{\rm H}$ of the dip is slightly higher than that of other phase intervals. Moreover, the covering fraction is significantly higher and it is 81 ± 3 per cent compared to 32 ± 4 per cent and 41 ± 4 per cent for the first and second maximum, respectively. We conclude that the dip in the pulse profile is likely produced by an increase in the extension and density of the localized absorbing region. This can also explains the lower X-ray flux level for $E < 1.5$ keV of the spectrum at the dip, compared with that of the two maxima. The spectra of three phase intervals have indeed comparable temperatures and consequently it is the partial covering component that produces a change in the spectral shape (see also Fig. 5). The normalization of the CEMEKL goes from a minimum of 0.0012 ± 0.0002 (pulse minimum) to a maximum of 0.0165 ± 0.0003 (first pulse maximum) following the X-ray flux trend. We found that $\tau_{\rm edge}$ is constant with respect to the phase within statistical uncertainty, while we found an indication that the equivalent width of the fluorescent Fe line could be variable. It goes from 0.11 ± 0.03 keV at the first maximum to 0.25 ± 0.06 keV at the dip. We note that the addition of a blackbody component is not required in any of the phase-resolved spectra.

3.4 The RGS spectrum

We extracted bright phase (phase approximately 0.35–0.95) spectra (0.028 ± 0.002 c s^{-1}, or 65 per cent of total, for RGS1; 0.038 ± 0.002 c s^{-1}, 74 per cent, for RGS2), with an exposure time of ∼19.6 ks. Both the phase-averaged and bright phase spectra are of comparable statistical quality, and the results of the spectral fits are identical, to within statistical errors. In fitting the RGS data, we grouped channels so that each has at least 16 source counts, used the C statistic as the fit statistic, but used χ^2 as the test statistic.

The low statistical quality of the RGS data places severe limitations on the inferences that we can draw from them. First, we

Table 3. Spectral parameters as a function of the phase. The interstellar absorption, the abundance and α are kept fix at their average spectral value: $N_{\rm Hp} = 0.033 \times 10^{22}$ cm^{-2}, $A = 0.71$ and $\alpha = 1.1$. Uncertainties are at 1σ confidence level.

	Spectrum as a function of the rotational phase								
Phase interval	$N_{\rm H_{Pc}}$ (10^{22} cm^{-2})	cvf (per cent)	$E_{\rm edge}$ (keV)	τ	$kT_{\rm max}$ (keV)	norm 10^{-2}	EW[a] (keV)	$F_{0.3-10}$ [b] 10^{-12} (erg cm^{-2} s^{-1})	χ^2_ν (dof)
Min ($\phi = 0.00 - 0.31$)	4.8 (fix) [c]	<50 [d]	0.70 (fix) [c]	<0.51 [d]	6.3 ± 0.7	0.12 ± 0.02	<0.68 [d]	0.85 ± 0.14	1.26 (156)
I Max ($\phi = 0.39 - 0.61$)	4.0 ± 0.7	32 ± 4	0.70 ± 0.01	0.50 ± 0.06	55 ± 10	1.65 ± 0.03	0.11 ± 0.03	14.0 ± 0.3	0.97 (747)
Dip ($\phi = 0.63 - 0.70$)	6.4 ± 0.8	81 ± 3	0.70 (fix) [c]	<1.30 [d]	$44\pm^{50}_{16}$	1.29 ± 0.08	0.25 ± 0.06	11.0 ± 0.7	1.07 (101)
II Max ($\phi = 0.76 - 0.93$)	3.1 ± 0.6	41 ± 4	0.69 ± 0.02	0.42 ± 0.08	$43\pm^{12}_{8}$	1.44 ± 0.04	<0.17 [d]	12.1 ± 0.4	1.00 (428)

Note: [a]The energy is fixed at 6.4 keV. [b]Unabsorbed 0.3–10 keV flux. [c]Value derived from the average spectrum. [d]3σ upper limit.

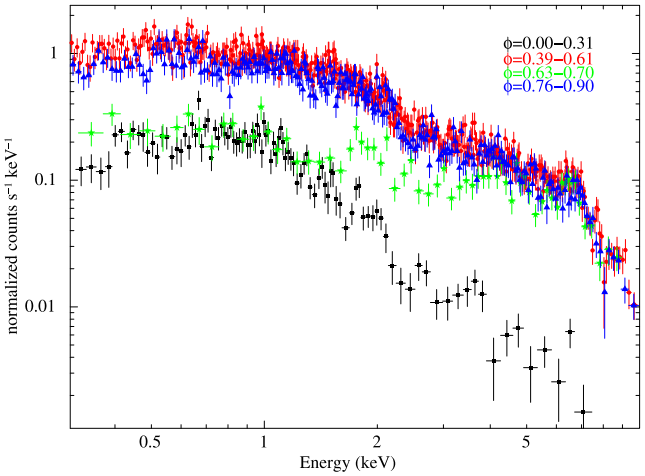

Figure 5. The EPIC-PN spectra as a function of the rotational phase: minimum (black), first maximum (red), dip (green), second maximum (blue). MOS1 and MOS2 spectra are not shown for plotting purposes.

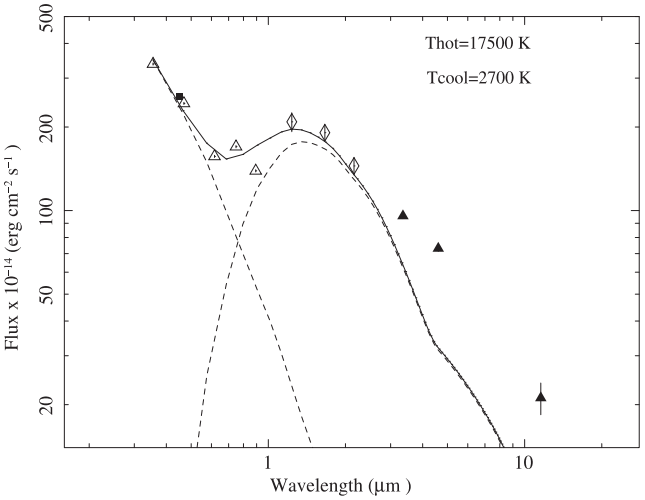

Figure 7. The SED constructed with the *XMM–Newton B*-band flux (filled square), the SDSS photometry (empty triangles), the 2MASS nIR (empty diamonds) and *WISE* measures (filled triangles). Correction for interstellar absorption has been applied. The dashed lines represents two blackbody components, while the solid line is the sum of the two.

investigated if we can confirm the presence of the absorption edge, using the best-fitting spectral model for the phase-averaged EPIC data (Table 2), minus the 6.4 keV line. We also compared the RGS data with this model, but without the edge. While the addition of this component improves the fit, even the model without the edge is statistically acceptable. Most importantly, from these low S/N RGS spectra, we cannot be certain that the addition of an edge, rather than some other changes e.g. in the complex absorber, is the best way to improve the model. Therefore, the comparison proved inconclusive.

We also investigated the emission lines in the RGS spectra. Two lines are securely detected: the O VIII line, whose laboratory energy is 0.654 keV (∼20 eV equivalent width) and the Ne X line expected at 1.021 keV (∼ 35 eV). In the bright phase spectra (Fig. 6), the Ne line has a much lower peak, which may be because it is somewhat broadened. Unfortunately, at the 90 per cent confidence limit, only upper limits to the physical widths can be determined ($\sigma < 2.6$ eV for the O line and <19 eV for the Ne line). The O VIII line is measured at $0.653\pm^{0.001}_{0.002}$ keV and Ne X line at $1.013\pm^{0.009}_{0.007}$ keV. These best-fitting line centroids are slightly redshifted compared to the laboratory values by ∼450 km s^{-1} for the O VIII line and ∼2000 km s^{-1} for the Ne X line, although the 90 per cent error ranges do (barely) overlap with the laboratory values. Further higher S/N observations

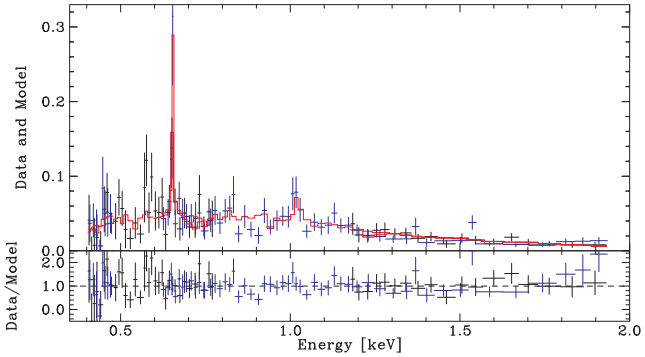

Figure 6. Lightly binned RGS spectra during the bright phase. The top panel shows the data and model (the best-fitting model for the average EPIC+BAT spectrum minus the Gaussian at 6.4 keV) the bottom panel the data to model ratio.

are mandatory to accurately estimate the redshift. In addition, the strength of the Ne line may indicate an overabundance of neon. Using the best-fitting EPIC model, replacing CEMEKL with CEVMKL and fixing all parameters other than the Ne abundance and the normalization, we obtain a Ne abundance of 2.3 ± 1.3, compared with 0.71 for other elements from the EPIC fit.

3.5 Spectral energy distribution

We also constructed a broad-band mid-IR and optical spectral energy distribution (SED). We used the average OM *B*-band flux, the SDSS u', g', r', i', z' magnitudes, as well as the 2MASS *J*, *H* and *K* measures and those from the *WISE* (Wright et al. 2010) in the *W1* (3.35 μm), *W2* (4.6 μm) and *W3* (11.6 μm) bands. We do not use the *W4* (22.1 μm) band as it only provides an upper limit.[1] We corrected the SED for interstellar absorption adopting $E(B-V) = 0.05$ corresponding to the column density of the total absorber found from X-ray spectral fits ($N_{\rm H} = 3.3 \times 10^{20}$ cm^{-2}). In Fig. 7, we report the SED. It cannot be reproduced by a single power law as the flux decays from the UV to the red, but increases at longer wavelengths. The blue portion of the SED alone cannot either be represented by the typical power law with index $\alpha \sim 0.5$, which is due to the combination of an optically thick and cyclotron (free–free) emissions (Harrison et al. 2013). We then tentatively describe the SED shape with two components consisting of a hot $T_{\rm h} = 17\,500 \pm 1500$ K and a cool $T_{\rm c} = 2700 \pm 300$ K blackbodies. The normalizations give, for a distance of 240 pc (see below), $R_{\rm h} = 6.5 \pm 0.8 \times 10^8$ cm and $R_{\rm c} = 2.0 \pm 0.7 \times 10^{10}$ cm. The former is of the order of WD radius and could be a mixture of contributions (see Section 4). The cooler component could be ascribed to the donor star. It is mainly responsible for the near-infrared (nIR) flux $\lambda < 1$ μm, but an excess is present at longer wavelengths ($\lambda > 3$ μm). We discuss this excess in Section 4.

[1] The SDSS data were taken in 2009 Oct, the 2MASS data in 1999, the *WISE* photometry in 2010 June and Dec.

4 DISCUSSION

The clear detection of strong X-ray pulsations (PF consistent with 100 per cent in the 5–12 keV) at the known orbital period of Swift J2218.4+1925 and the absence of any other periodic signal (e.g. from an asynchronous WD rotation period) confirms the recent proposal that this hard-X-ray CV is a magnetic system of the polar type. The 2.16 h orbital period locates this binary just at the lower edge of the orbital period gap and well within the range of bulk of polars (Beuermann 1999; Townsley & Gänsicke 2009). We discuss in the following the main results of our analysis.

4.1 The orbital variability

The X-ray light curve folded at the orbital period reveals the typical bright and faint phases of the magnetic polar-type CVs. These are due to the post-shock accretion flow above the main (upper) pole coming into (bright phase) and out of view (faint phase) if the magnetic axis is tilted with respect to the rotation axis (β) and shifted in azimuth (ψ). Here, β is the magnetic colatitude and ψ is the angle between the line of centres of stellar components and the projection of the magnetic axis on the orbital plane (see Cropper 1988). The length of the faint phase is used to restrict the range of binary inclination i and β (Cropper 1990). The presence of one bright phase implies $i + \beta \geq 90^\circ$. The absence of eclipses implies $i \leq 75^\circ$. Thorstensen & Halpern (2013), adopting $M_{\rm WD} = 0.75\,{\rm M}_\odot$ and $M_2 = 0.2\,{\rm M}_\odot$ for the WD and companion masses, suggest $i = 50^\circ$. We extend the orbital inclination to $i = 42^\circ$, as the WD mass is found to be larger (see below). The faint phase lasts $\Delta\phi \sim 0.3$, giving $\beta \sim 55^\circ$–64° for $i \sim 40^\circ$–50°. Furthermore, the rapid rise and decay of the bright phase can be used to estimate the extent of the X-ray emitting region. They both last $\sim$500 s which would imply an azimuthal extent of the spot on the WD of $\sim 24^\circ$ assuming no lateral extent. This translates into a fractional circular spot area $\sim 0.045\ A_{\rm WD}$, where $A_{\rm WD}$ is the total WD area.

The X-ray bright phase is characterized by a narrow (width $\sim$0.1) dip that is energy dependent due to absorbing material above the X-ray emitting region. A dip due to the accretion stream at the threading of the magnetic field lines would imply $i > \beta$, but we find it is not the case. The only absorbing material that would produce such a feature should be located in the accretion pre-shock flow (Done & Magdziarz 1998). This feature is also observed at hard X-rays >5 keV. At these energies it cannot be due to absorption. It has been observed in a few other polars and explained as due to occultation by the dense core of the channelled accretion flow (Ramsay et al. 2004b). The shifts observed in the time occurrence of the dip during the *XMM–Newton* observation also suggest changes in the local mass accretion rate. This is also seen in other few polars (Harrop-Allin et al. 1999; Schwope et al. 2001). Due to the lack of eclipses and the impossibility to link the spectroscopic ephemeris by Thorstensen & Halpern (2013) with our epoch, we cannot constrain the azimuth ψ of the accreting region.

The 0.3–12 keV X-ray light curve during the faint phase does not reach zero counts. This implies that there is an additional contribution, likely the secondary pole, that comes into view as the WD rotates. The spectrum of the faint phase indicates that this pole has a softer emission. This is not unusual in the polars, where the main pole is harder than the other one (Beuermann 1999).

The *B*-band light curve also displays a bright phase, which is almost in phase with the X-rays as well as the dip feature, although the rise leads the X-rays by $\sim$700 s. The optical emission in polars can be due to several contributions, such as cyclotron emission, the accretion stream, the accretion heated WD spot as well as the unheated WD photosphere. These are difficult to disentangle without polarimetric and multicolour photometric data. Cyclotron beaming is expected to be antiphased with respect to the X-rays since the maximum cyclotron flux is emitted perpendicularly to the field lines (Cropper 1988, 1990; Burwitz et al. 1998; Matt et al. 2000). An upper limit to the contribution of cyclotron flux can be derived from the flux difference at maximum and minimum of optical light curve. If the variability is totally due to cyclotron, we derive $F_{\rm cyc}/F_{\rm X} < 0.11$, indicating that cyclotron is not the main cooling mechanism in Swift J2218.4+1925. The *B*-band light curve has a smoother rise and lower amplitude than the X-rays, which suggests a larger emitting area and being due to reprocessing (see also Vogel et al. 2008). The broad-band SED indicates a mildly hot component contributing to the blue portion. This comprises of the variable and stationary components, which we cannot disentangle due to the lack of phase-resolved colour photometry. The presence of the dip in the optical with similar width as that in the X-rays, further indicates that the dense parts of the accretion flow are responsible for this feature also in the optical. Polarimetry and colour-photometry are then essential to identify the origin of the optical variability.

4.2 The spectral characteristics

The X-ray analysis reveals an average hard-X-ray spectrum with maximum temperature $kT = 37$ keV. This is consistent with the typical temperature of magnetically confined accretion flows, where a shock region is formed above the poles of the WD. $kT_{\rm max}$ must be regarded as a lower limit of the maximum temperature of the post-shock region, which strongly depends on the WD mass (Aizu 1973). We also note that the presence of the Fe line at 6.4 keV would require a reflection component above 10 keV (Done, Osborne & Beardmore 1995). Its inclusion would lower the maximum temperature. However, due to the low S/N of the data above 10 keV, this component is not required in the fit. Furthermore, the lack of a detectable soft blackbody component and the fact that this polar is a strong hard-X-ray emitter with respect to other polars (see also below) allows us to use the X-ray temperature to estimate the WD mass. In particular, we use the dedicated model of Suleimanov, Revnivtsev & Ritter (2005)[2] developed for bremsstrahlung-dominated magnetic CVs and in particular for IPs. The model accounts for the growth of pressure towards the WD surface and hence the change of gravity. This allows us to get a more reliable estimate of the maximum temperature and, consequently, a more solid estimate of the WD mass. The model is computed for the continuum only, consequently we added a broad Gaussian to account for the iron complex (thermal and fluorescence) centred at 6.68 ± 0.03 keV and with EW $= 0.53 \pm 0.07$ keV. A fit to the *XMM–Newton* EPIC and Swift BAT spectrum for $E > 3$ keV gives $M = 0.99\,^{+0.09}_{-0.14}\ {\rm M}_\odot$, but the fit quality is slightly low ($\chi^2_\nu = 1.15$). As a cross-check, we also derived the WD mass from the temperature of the spectrum at the first maximum, $kT_{\rm max} = 55 \pm 10$ keV, and we get $M_{\rm wd} = 0.97 \pm 0.08\,{\rm M}_\odot$ (see Aizu 1973, for more details). This is fully consistent with what derived from the dedicated model. Such a WD would have a radius of $R_{\rm wd} = 0.57 \pm 0.06 \times 10^9$ cm.

The spectral analysis also show the presence of high column density material (~ 3–6×10^{22} cm^{-2}), which partially absorbs the X-ray emission. This material is located in the pre-shock flow above the WD pole and is the main responsible in producing the pulse dip.

[2] This is a private code that runs into XSPEC.

There is an indication that the EW of the fluorescent Fe line at 6.4 keV could changes with the phase, being slightly larger in the dip than at the maximum of the pulse profile. This could indicate that the Fe line is less sensitive to orbital variations than the continuum. Whether it forms at the WD surface or/and in the pre-shock flow cannot be assessed without knowledge of a reflection component at hard X-rays, which is expected to be present along the fluorescent iron line (Done et al. 1995).

Particularly interesting is the detection in the EPIC spectra of ionized absorbing material that produces an absorption feature at ∼0.7 keV. This energy might be consistent with an absorption edge of O VII. Unfortunately, we cannot confirm this feature in the RGS due to the poor S/N. An oxygen edge has been observed in a few IPs (Mukai et al. 2001; de Martino et al. 2008; Bernardini et al. 2012) and commonly in the low-mass X-ray binaries dippers. If due to oxygen Swift J2218.4+1925 would be the first polar showing such feature. The ionization state in the pre-shock flow depends on the ratio of matter density in the pre-shock to the radiation density emitted in the post-shock regions. A low level of ionization is expected if cyclotron, which is emitted in a non-ionizing form, is the dominant cooling mechanism or if the shock is taller than wide. In tall shocks a large fraction of X-rays are emitted perpendicularly to the field lines. Hence, both the evidence of a warm absorber and the indication of a large extent of the accretion spot in Swift J2218.4+1925 would corroborate a high-ionization state in the pre-shock flow. This in turn would also suggest that cyclotron is not the dominant cooling mechanism, likely due to a low-magnetic field WD.

The SED also reveals a cool ($T_c \sim 2700$ K) emission from the companion star. We note an excess of flux in the *WISE* bands for $\lambda > 3\,\mu$m. Another argument favouring an extra mid-IR component is that time-resolved *WISE* photometry (see Fig. 8) shows a large variability $\Delta m \sim 1.6$ that cannot be due to ellipsoidal modulation of the donor star (typically less than 0.1 mag). However, caution has to be taken, because *WISE* and 2MASS data are taken 10 years apart. A mid-IR excess is questioned to be due to dust by circumstellar discs or by cyclotron from the accretion region. A circumbinary disc would not give rise to any variability and; therefore, the mid-IR excess is very likely due to cyclotron emission. Similar behaviour was found for AM Her and EF Eri and the few polars observed in the mid-IR (Brinkworth et al. 2007; Harrison et al. 2013), indicating that low cyclotron harmonics ($n = 1, 2, 3$), at these wavelengths, are optically thin. Both polars share a low magnetic field strength ($B \sim 1.3 \times 10^7$ G). The lack of nIR and IR spectroscopy does not allow a meaningful analysis with cyclotron models for Swift J2218.4+1925.

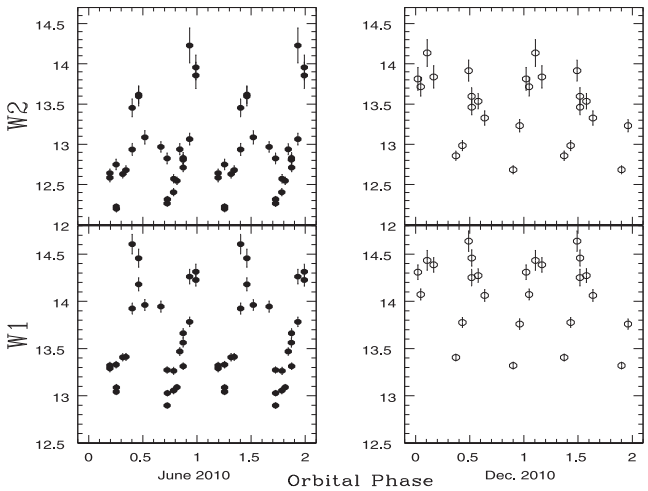

Figure 8. The *WISE* light curve constructed using the 'single exposures' in the *W*1 and *W*2 bandpasses for the two epochs (2010 June and Dec) showing large IR variability. The orbital phases are computed using arbitrary zero times. Ordinates are in magnitudes.

For an orbital period of 2.16 h, the secondary star is expected to be of spectral type M4 V, $T_{\rm eff} = 3300$ K (Knigge 2006). The temperature we derived from the SED is compatible within 2σ with this value. The 2MASS $(J - H)$ colour corrected for interstellar extinction is 0.70 ± 0.11 mag. This is consistent, within uncertainties, with that expected for a M4 V star, $(J - H)_{\rm o} = 0.57$ (Knigge 2006; Straižys & Lazauskaitė 2009). Using an M4 V star absolute magnitudes $M_J = 8.45$ and $M_K = 7.60$ (Knigge 2006) and assuming that it contributes 82 and 89 per cent to the observed flux in these bands, as derived from the SED, we estimate a distance of 230–250 pc, respectively.

4.3 The energy balance

We now estimate the mass accretion rate and verify if it is consistent with that expected for a binary evolving through gravitational radiation. For a donor star mass $M_2 = 0.2\,{\rm M}_\odot$, the binary mass ratio is $q = 0.2$ and for $P_{\rm orb} = 2.16$ h the expected secular mass transfer rate for gravitational losses (Warner 1995) is $\dot{M} \sim 4 \times 10^{-11}\,{\rm M}_\odot\,{\rm yr}^{-1}$. At a distance of 230–250 pc the bolometric X-ray luminosity is $L_{\rm X} = 1.1 \pm 0.1 \times 10^{32}\,{\rm erg\,s}^{-1}$. Assuming it represents the accretion luminosity, for a WD mass 0.97 $\rm M_\odot$, we obtain that the mass accretion rate is $\dot{M} \gtrsim 8 \times 10^{-12}\,{\rm M}_\odot\,{\rm yr}^{-1}$. We conclude that, despite the uncertainties on the true total accretion luminosity, the mass accretion rate is consistent with a binary evolving through gravitational radiation.

The lack of a soft (20–50 eV) blackbody component in the X-ray spectrum, could arise by the large accretion footprints that would shift the reprocessed radiation to EUV, FUV wavelengths. *XMM–Newton* observations have shown that a large fraction (∼40 per cent) of polars when accreting at high rate do not exhibit a detectable soft blackbody component (Ramsay & Cropper 2004a). This suggests selection effects in source detection due to soft-band coverage of previous X-ray surveys (e.g. *ROSAT*; Beuermann 1999). Swift J2218.4+1925 thus adds to this group. However, as pointed out by Ramsay et al. (2009), there is no obvious explanation on why these hard polars should have larger accretion areas than the other polars since neither the orbital period nor magnetic field strengths of the two groups are so different.

The hard X-ray detection of Swift J2218.4+1925 also poses the question on whether the few hard-X-ray-selected polars possess lower magnetic fields and/or more massive WDs. To date, 11 systems have been detected in the *Swift* and *INTEGRAL* surveys with a few asynchronous ones. These do not seem to share similar magnetic field strengths and masses (de Martino, in preparation). Swift J2218.4+1925 is found to have a moderately massive WD. Whether its magnetic field is low, it should be assessed with future polarimetric observations.

5 SUMMARY

We studied Swift J2218.4+1925, a candidate CV of the polar type. The main goal of this research is to unambiguously unveil the source real nature and characterize its broad-band properties. For this purpose, we used X-ray and optical *XMM–Newton* data, together with non-simultaneous high-energy coverage provided by *Swift* BAT and

ground-based optical, near and mid-IR data. The main results are briefly summarized in the following.

(i) We measure a X-ray period of 2.16 h, fully consistent with that derived from optical spectroscopy, thus allowing us to identify Swift J2218.4+1925 as a CV of the polar type.

(ii) The source shows a longer bright and a shorter faint phase with a prominent dip between the two, both in the X-ray and in the optical band. The pulse shape changes with the energy, and the dip is more pronounced at lower energy. The PF strongly increases with the energy interval being consistent with 100 per cent at high energies. These are all typical characteristics of polars.

(iii) We infer an orbital inclination $i \sim 40^\circ$–50°, a magnetic co-latitude $\beta \sim 55^\circ$–64° and a large accretion spot azimuth $\sim 24^\circ$.

(iv) The X-ray emission originates in the post-shock flow reaching a maximum temperature of ~ 55 keV and is heavily absorbed by high-density material in the pre-shock flow. We derive a WD mass of 0.97 ± 0.08 $M_\odot$. The lack of a soft X-ray blackbody component adds Swift J2218.4+1925 to the increasing group of polars without a detectable reprocessed X-ray component.

(v) An intense fluorescent Fe line at 6.4 keV is present whose equivalent width changes along the orbital cycle.

(vi) An absorption edge at 0.70 keV possibly due to O VII, reveals for the first time the presence of a warm absorber in a polar.

(vii) We found indication of an overabundance of neon and a possible indication of redshift of the O VIII and Ne X lines of about 450–2000 km s^{-1}.

(viii) The optical to mid-IR SED is described with two blackbody components at $\sim$18 000 K and at $\sim$ 2700 K. While the former could be a mixture of contributions difficult to assess with the present data, the cool component is ascribed to the donor star of M4 V spectral type. A mid-IR excess also suggests the presence of an extra component, possibly due to emission from lower cyclotron harmonics. We also estimate a distance of 230–250 pc.

ACKNOWLEDGEMENTS

This work is based on observations obtained with *XMM–Newton* an ESA science mission with instruments and contributions directly funded by ESA Member States; with *Swift*, a National Aeronautics and Space Administration (NASA) science mission with Italian participation. This publication also makes use of data products from the *WISE*, which is a joint project of the University of California, Los Angeles, and the Jet Propulsion Laboratory/California Institute of Technology, funded by the NASA; the 2MASS, a joint project of the University of Massachusetts and the Infrared Processing and Analysis Center (IPAC)/Caltech, funded by NASA and the NSF; and the SDSS.

FB acknowledge the Galileo Galilei Institute for Theoretical Physics for the hospitality and the INFN for partial support during the completion of this work, and thank Dr Giorgio Lanzuisi for his precious suggestions concerning Monte Carlo simulations. DdM and FB acknowledge financial support by ASI under contract ASI-INAF I/037/12/0.

REFERENCES

Aizu K., 1973, Prog. Theor. Phys., 49, 1184
Anzolin G., de Martino D., Bonnet-Bidaud J.-M., Mouchet M., Gänsicke B. T., Matt G., Mukai K., 2008, A&A, 489, 1243
Anzolin G., de Martino D., Falanga M., Mukai K., Bonnet-Bidaud J.-M., Mouchet M., Terada Y., Ishida M., 2009, A&A, 501, 1047
Barlow E. J., Knigge C., Bird A. J., J Dean A., Clark D. J., Hill A. B., Molina M., Sguera V., 2006, MNRAS, 372, 224
Barthelmy S., 2000, in Flanagan K. A., Siegmund O., eds, Proc. SPIE Conf. Ser. Vol. 4140, X-ray and Gamma-Ray Instrumentation for Astronomy XI. SPIE, Bellingham, p. 50
Baumgartner W., Tueller J., Markwardt C., Skinner G., Barthelmy S., Mushotzky R., Evans P., Gehrels N., 2013, ApJS, 297, 19
Bernardini F. et al., 2009, A&A, 498, 195
Bernardini F., de Martino D., Falanga M., Mukai K., Matt G., Bonnet-Bidaud J.-M., Masetti N., Mouchet M., 2012, A&A, 542, A22
Bernardini F. et al., 2013, MNRAS, 435, 2822
Beuermann K., 1999, in Aschenbach B., Freyberg M. J., eds, Highlights in X-ray Astronomy. Max-Planck-Institut für extraterrestrische Physik, Garching, p. 410
Bird A. J. et al., 2010, ApJS, 186, 1
Brinkworth C. et al., 2007, ApJ, 659, 1541
Burwitz V. et al., 1998, A&A, 331, 262
Cropper M., 1988, MNRAS, 231, 597
Cropper M., 1990, Space Sci. Rev., 54, 195
Cusumano G. et al., 2010, A&A, 524, A64
de Martino D. et al., 2008, A&A, 481, 149
den Herder J. W. et al., 2001, A&A, 365, L7
Dickey J. M., Lockman F. J., 1990, ARA&A, 28, 215
Done C., Magdziarz P., 1998, MNRAS, 298, 737
Done C., Osborne J., Beardmore A., 1995, MNRAS, 276, 483
Harrison T., Hamilton R., Tappert C., Hoffman D., Campbell R., 2013, AJ, 145, 19
Harrop-Allin J., Cropper M., Hakala P., Hellier C., Ramseyer T., 1999, MNRAS, 308, 807
Kalberla P. M. W., Burton W. B., Hartmann D., Arnal E. M., Bajaja E., Morras R., Pöppel W. G. L., 2005, A&A, 440, 775
Knigge C., 2006, MNRAS, 373, 484
Lanzuisi G. et al., 2013, ApJ, 778, 62
Masetti N. et al., 2008, A&A, 482, 113
Masetti N. et al., 2010, A&A, 519, A96
Masetti N. et al., 2012a, A&A, 538, A123
Masetti N., Nucita A., Parisi P., 2012b, A&A, 544, A114
Mason K. O. et al., 2001, A&A, 365, L36
Matt G., de Martino D., Gäensicke B., Negueruela I., Bonnet-Bidaud J.-M., Mouchet M., Mukai K., 2000, A&A, 358, 177
Mukai K., Kallman T., Schlegel E., Bruch A., Handler G., Kemp J., 2001, in Inoue H., Kunieda H., eds, ASP Conf. Ser. Vol. 251, New Century of X-ray Astronomy. Astron. Soc. Pac., San Francisco, p. 90
Muno M. P. et al., 2004, ApJ, 613, 326
Ramsay G., Cropper M., 2004a, MNRAS, 347, 497
Ramsay G., Bridge C., Cropper M., Mason K., Cordova F., Priedhorsky W., 2004b, MNRAS, 354, 773
Ramsay G., Rosen S., Hakala P., Barclay T., 2009, MNRAS, 395, 416
Revnivtsev M., Sazonov S., Churazov E., Forman W., Vikhlinin A., Sunyaev R., 2009, Nature, 458, 1142
Revnivtsev M., Sazonov S., Forman W., Churazov E., Sunyaev R., 2011, MNRAS, 414, 495
Sazonov S., Revnivtsev M., Gilfanov M., Churazov E., Sunyaev R., 2006, A&A, 450, 117
Schwope A., Schwarz R., Sirk M., Howell S., 2001, A&A, 375, 419
Straižys V., Lazauskaitė R., 2009, Balt. Astron., 18, 19
Suleimanov V., Revnivtsev M., Ritter H., 2005, A&A, 435, 191
Thorstensen J., Halpern C., 2013, AJ, 146, 107
Townsley D., Gänsicke B., 2009, ApJ, 693, 1007
Turner M. J. L. et al., 2001, A&A, 365, L27
Ubertini P. et al., 2003, A&A, 411, L131
Vogel J., Byckling K., Schwope A., Osborne J., Schwarz R., Watson M., 2008, A&A, 485, 787
Warner B., 1995, Cambridge Astrophysics Series, 28: Cataclysmic Variable Stars. Cambridge Univ. Press, Cambridge
Wright E. L. et al.2010, AJ, 140, 1868

This paper has been typeset from a TEX/LATEX file prepared by the author.